Research Article Vol. 33, No. 8 / 21 Apr 2025 / Optics Express 17886
Optics EXPRESS

Gratings for multi-resolution edge illumination X-ray phase contrast imaging: concept and simulation

PIETER-JAN VANTHIENEN,[1,2,*] NICHOLAS FRANCKEN,[1,2] JONATHAN SANCTORUM,[1,2] JAN SIJBERS,[1,2] AND JAN DE BEENHOUWER[1,2]

[1] *imec-Vision Lab, Dept. of Physics, University of Antwerp, Universiteitsplein 1, 2610 Antwerpen, Belgium*
[2] *DynXlab: Center for 4D Quantitative X-ray Imaging and Analysis, Universiteitsplein 1, 2610 Antwerpen, Belgium*
[*] *pieter-jan.vanthienen@uantwerpen.be*

Abstract: Edge illumination (EI) is an established X-ray phase-contrast imaging method that relies on gratings to obtain attenuation, differential phase, and dark field contrast. Conventional gratings with one-dimensional line apertures, however, pose a major limitation in geometric flexibility of current EI-setups. That is, the gratings are designed for a fixed magnification and the period and aperture size of the gratings determine the fixed resolution. Changing the magnification can adjust the resolution, since the sample is projected over a smaller or larger detector area, but even a small change in magnification causes a mismatch between beamlets and pixels. To allow multi-resolution EI from a single experimental configuration, a grating which retains the projected period at different magnifications is required. In this paper, a trapezoidal grating that overcomes these limitations is studied using Monte Carlo and ray-tracing simulations, including a flat field experiment, a peak-to-peak contrast-to-noise ratio experiment, and EI scans of test phantoms. This simulation study demonstrates the concept of multi-resolution EI and shows its potential towards a generic and flexible EI setup.

1. Introduction

Edge illumination (EI) [1] is an X-ray phase-contrast (XPC) imaging technique that allows imaging a sample based on three complementary contrasts: attenuation, phase, and dark field contrast. EI is a grating-based method, which in contrast to other X-ray phase contrast methods, like Bonse-Hart interferometry [2], analyzer-based imaging [3], or free-space propagation [4], does not require coherent illumination [5]. Compared to other grating-based XPC techniques, like grating based interferometry, shearing interferometry [6], and Talbot-Lau interferometry [7], EI is a non-interferometric method which has a relatively simple setup, can more easily be scaled up in size, and is more robust to mechanical vibrations or imperfections [8]. These advantages create potential for EI in various applications, such as medical imaging [9,10], security [11], historical studies [12], materials science [13,14], and the food industry [15].

To capture a two-dimensional X-ray image, a setup consisting of an X-ray source, sample stage, and detector is required. To extend to computed tomography, which reveals three- dimensional information, the sample must be placed on a rotating stage. In Fig. 1, a typical edge illumination X-ray computed tomography (EIXCT) setup is depicted. Compared to a conventional X-ray radiography setup, two additional optical components are added: the sample grating and the detector grating [16]. The sample grating is positioned in front of the sample to split the X-ray cone-beam into beamlets. The detector grating is positioned in front of the detector to create insensitive regions between adjacent pixels on the detector, which allows to measure changes in direction of the beamlets. Since EI does not rely on interference, the apertures are separated by

#550252 https://doi.org/10.1364/OE.550252
Journal © 2025 Received 9 Dec 2024; revised 1 Apr 2025; accepted 3 Apr 2025; published 15 Apr 2025

Optics EXPRESS

a sufficiently large distance avoiding mutually interfering beamlets. As such, the refraction of individual beamlets can be determined, which eliminates the requirement of a coherent source [5].

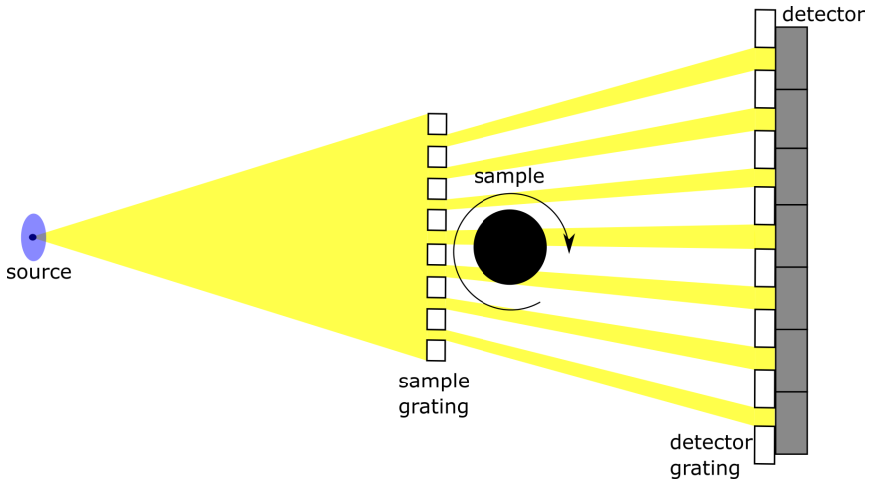

Fig. 1. The conventional cone-beam EI setup (not to scale). If the sample is placed on a rotational stage, EIXCT can be acquired.

While most edge illumination setups use planar gratings with rectangular and equally wide apertures [17,18], alternative grating designs have been proposed in literature. Examples of such designs include L-shaped apertures, which allow to measure 2D phase sensitivity [19], skipped gratings, which avoid pixel cross-talk [20], asymmetric gratings, which allow inline acquisitions [21], and gratings which reduce shadowing, like a combination of two tilted conventional gratings, curved gratings, or planar gratings with fan-shaped apertures [22].

While EI is an established XPC method, conventional gratings pose a major limitation on geometric flexibility. Conventional gratings consist of highly absorbing material with periodic one-dimensional line apertures. The gratings are custom made for a specific imaging geometry and perfectly positioned to align the two gratings with the detector pixels columns. The resolution for a setup is fixed and determined by the period of the sample grating. This resolution can be increased to the size of the aperture by using dithering. When dithering is applied, multiple projections are acquired for sub-pixel movements of the sample, hereby imaging the part of the sample that is not illuminated by the beamlets, and stitching the consequent images together [23,24]. To adjust the spatial resolution in conventional attenuation-based cone-beam X-ray imaging, where the setup is composed of only a source, sample, and detector, the object is usually positioned closer to or further away from the source, projecting the phantom onto a larger or smaller detector area. Unfortunately, this is not possible with conventional EI gratings. To achieve optimal phase and dark field sensitivity, the sample must be positioned as close as possible to the sample grating. Changing the image resolution requires that the sample grating moves along the optical axis with the sample, but even a small change in magnification causes a mismatch between beamlets and pixels, as shown in Fig. 2. While gratings divided into sections with different periods or apertures exist [20,25], the resolution can only be modified to discrete steps, and increasing the number of resolution steps comes at the expense of the field of view (FOV) or the grating size. To adjust the sample grating magnification while preserving the projected beamlet positions, a sample grating which retains the projected aperture period over a continuous range of magnifications is required, which is non-existent to our knowledge. Furthermore, while multi-resolution imaging is being thoroughly researched in various XPC

Optics EXPRESS

techniques (edge illumination, grating based interferometry, propagation-based imaging,. . .) [26–29], there is no laboratory XPC setup that allows to change the resolution over a continuous range of resolutions.

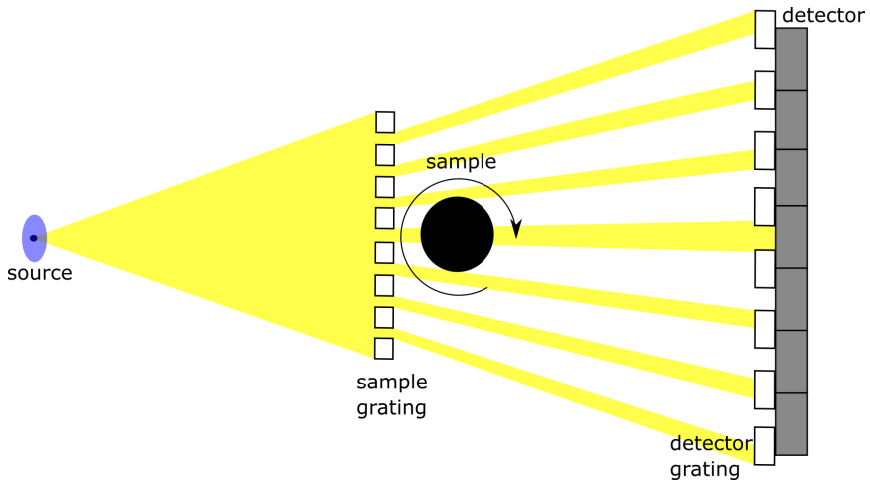

Fig. 2. The misaligned gratings and detector that occurs when the sample grating and the object are positioned closer to the source. Note that every newly formed beamlet is slightly displaced, which causes neighboring pixels to be illuminated differently.

In this manuscript, we expand on our prior work [30] by studying a trapezoidal sample grating, which allows to change the effective period of the sample grating by translating it vertically, thereby enabling multi-resolution EI acquisitions from a single experimental configuration, i.e., no optical elements need to be changed. To allow imaging on a 2D detector grid, the grating is rotated around the axis perpendicular to the aperture slits and perpendicular to the optical axis. The approach is demonstrated with a simulation study of a test-phantom imaged at different magnifications.

2. Methodology

2.1. Edge illumination

A typical setup for EI with a cone-beam source is shown in Fig. 1. Due to the aperture sizes and the distance between the apertures of the gratings, EI can be described using the ray-optical approach, where phase effects are represented by refraction of X-rays in an object, rather than the more rigorous Fresnel-Kirchoff diffraction theory [31–34]. The gratings transform refraction effects into intensity modulations at the detector, thereby providing phase-sensitivity. This modulated intensity signal contains information from attenuation, phase, and dark field contrast. Attenuation contrast images the difference in X-ray absorption of each beamlet by the sample, phase contrast is a measure for the difference in refraction of each beamlet by the sample and dark field contrast images the ultra-small angle scattering of the beamlet by the sample [13]. These three types of contrast can be separated using mask-stepping. In mask-stepping, the intensity at every pixel is measured while shifting the sample grating. These consecutive measurements result in the so-called illumination curve (IC) [35,36], which is approximately Gaussian. (cfr Fig. 3)

Comparing the ICs of a scan without sample (the flat field) and a scan with sample allows one to separate the three types of contrast. The attenuation contrast is retrieved from the difference in area under the ICs, phase contrast is retrieved from the difference in position of the maxima

Optics EXPRESS

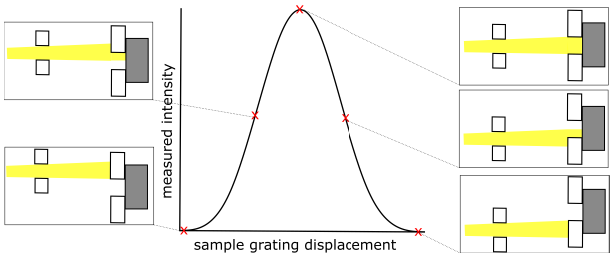

Fig. 3. An illumination curve using five mask-steps. The intensity is measured for different sample grating displacements and a Gaussian curve is fitted to the data points.

of the ICs, and dark field contrast originates from the broadening of the IC. The three different types of contrast are illustrated in Fig. 4.

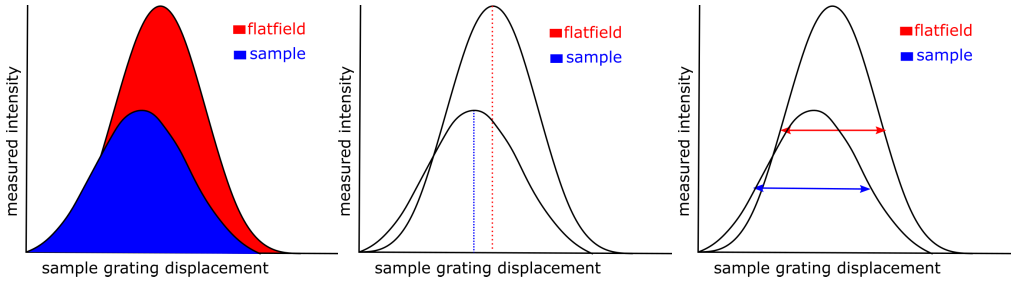

(a) Attenuation contrast. (b) Phase contrast. (c) Dark field contrast.

Fig. 4. The three different contrast types that can be derived from IC comparison.

2.2. *Multi-resolution EI*

The trapezoidal sample grating is shown in Fig. 5. The grating bars and apertures linearly diverge from the top to the bottom. Vertically translating the grating causes a change in grating period, as shown in Fig. 6. When the sample and the sample grating are translated along the optical axis, the magnification changes. To ensure that the gratings are properly aligned, and avoid a different illumination of the pixels as in Fig. 2, a different sample grating period is required at the new grating position. To preserve the projected period, for a system with a fan-beam source with a line detector, the trapezoidal sample grating is translated vertically. Translating the grating along the optical axis and preserving the projected period allows to image a section of the phantom at different resolutions, giving the opportunity to balance between field of view (FOV) (Fig. 7(a)) and resolution (Fig. 7(b)).

To allow imaging on a 2D detector grid, a carefully designed trapezoidal grating can be tilted around the mask-stepping axis. This concept is shown in Fig. 8. Tilting the gratings allows to align the sample grating for the pixel rows above and underneath the focused row. The tilting angle is dependent on the design parameters of the setup, which also determine the FOV and resolution range. The spatial relationships of an EI setup are shown in Fig. 9.

The trapezoidal grating is perfectly aligned in point B. To find the angle θ that aligns the tilted grating in point F, the intersection between the grating (BF) and the outer beamlet (AD), as shown in Fig. 9, we construct two expressions for the grating aperture period in this point F. The first expression $p_{F1}(\theta)$ defines the grating period required in point F, to comply with the changing magnification when tilting the grating. Point A represents the source, points C & D the boundaries of the detector onto which the grating is aligned. Line segment $[AD]$ correspond to

Optics EXPRESS

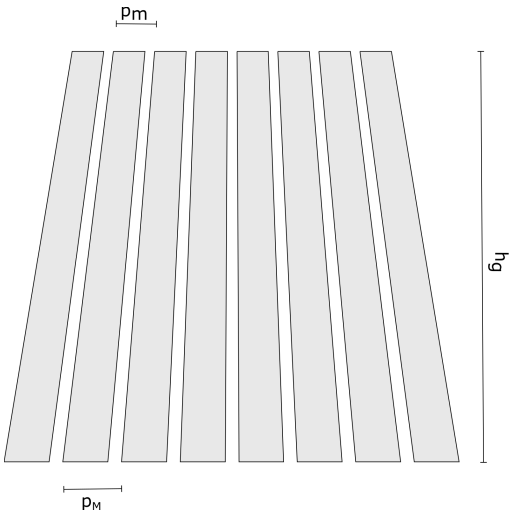

Fig. 5. The trapezoidal grating and its design parameters.

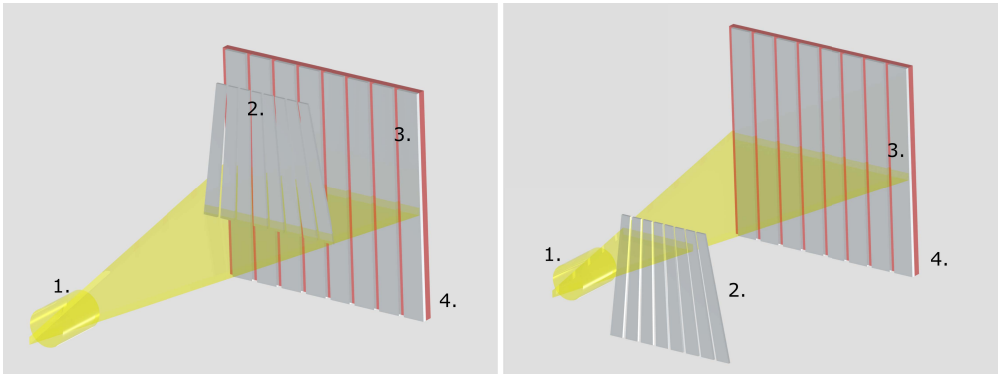

(a) EI setup with lower resolution and higher FOV. (b) EI setup with higher resolution and smaller FOV.

Fig. 6. 3D representation of the EI setup with a trapezoidal grating. 1. source 2. trapezoidal sample grating 3. detector grating 4. detector.

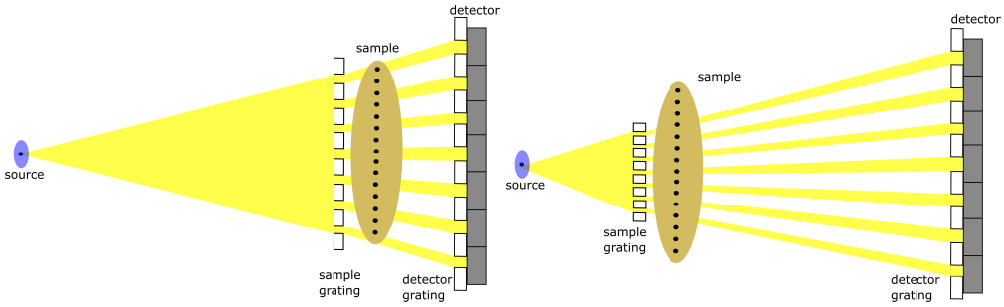

(a) EI setup with lower resolution and higher FOV. (b) EI setup with higher resolution and smaller FOV.

Fig. 7. EI setup with a trapezoidal grating.

Optics EXPRESS

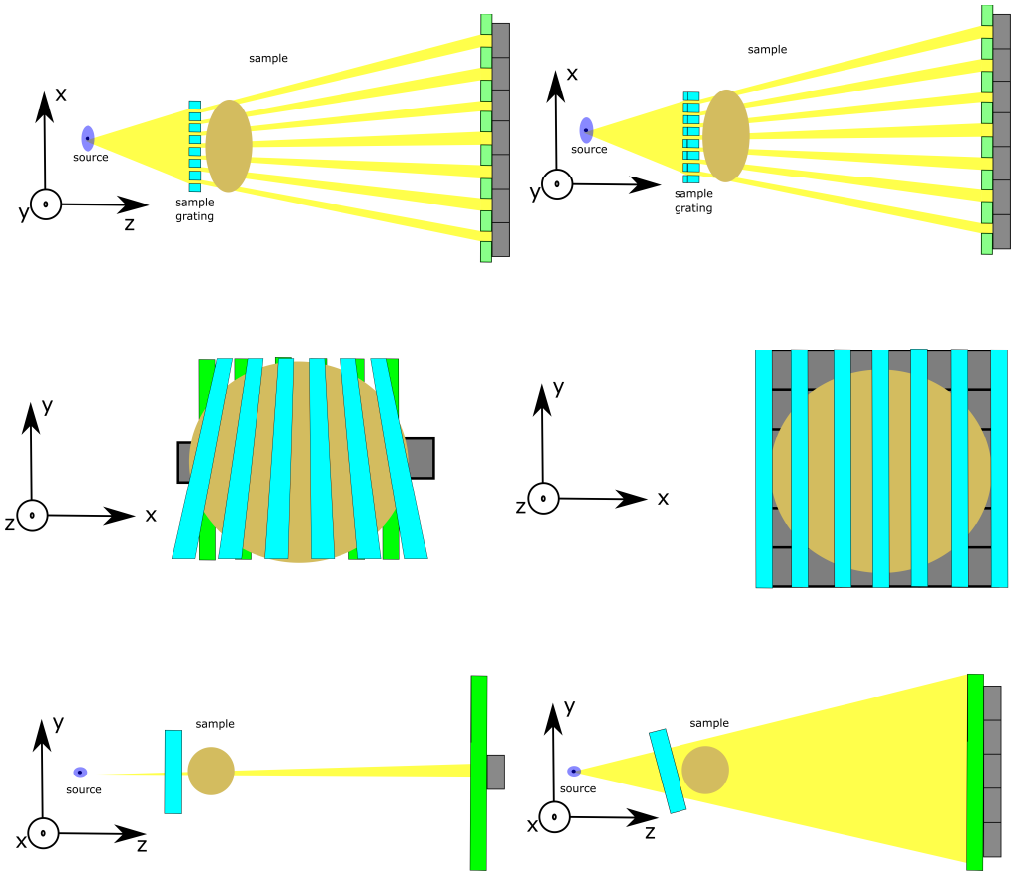

(a) Untilted setup with single row of detector pixels. (b) Tilted setup with multiple rows of detector pixels.

Fig. 8. Threefold view of a tilted and untilted EI setup. Note the change in axes orientation in the different image rows.

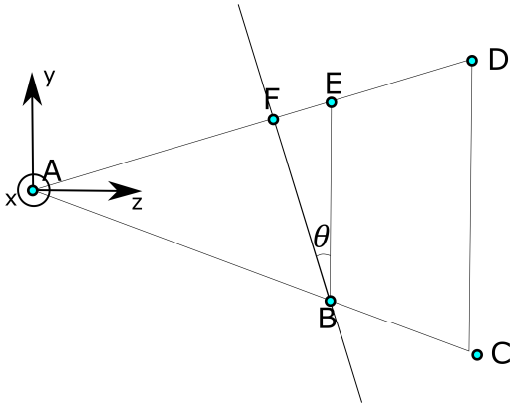

Fig. 9. The spatial relationships of an EI setup. Point A represents the source, points C & D the boundaries of the detector onto which the grating is aligned. Line segments $[AD]$ and $[AC]$ correspond to the outer beamlets. The trapezoidal grating is aligned in point B, and point E represents the intersection between the untilted grating, and the most outward beamlet $[AD]$. When the grating is rotated over an angle θ, point F corresponds the intersection of the tilted grating and the most outward beamlet.

Optics EXPRESS

the outer beamlet, and $[AF]$ to the line segment between the source point (A) and the point of alignment (F), as shown in Fig. 9. The pixel size p and $|AD|$ are fixed setup parameters.

$$p_{F1}(\theta) = p \cdot \frac{|AF|}{|AD|}. \tag{1}$$

The second expression $p_{F2}(\theta)$ is the grating period of the trapezoidal grating that is obtained in point F. By rotating the grating, the intersection point F shifts along AD and BF, resulting in a different period in F on the trapezoidal grating. $[BF]$ corresponds to the line segment between the original aligned point (B) and the point to be aligned by tilting (F), as shown in Fig. 9.

$$p_{F2}(\theta) = p_B + |BF| \cdot g. \tag{2}$$

The period in B (p_B) is again determined by the setup, and g is a design factor of the trapezoidal grating which defines the diverging of the trapezoidal grating bars. This parameter g is defined as $\frac{p_M - p_m}{h_g}$, with p_M the largest period on the grating, p_m the smallest period on the grating, and h_g the height of the grating, as shown in Fig. 5.

The appropriate angle to align the grating can then be computed by solving the equation $p_{F1}(\theta) = p_{F2}(\theta)$, which can be solved for θ as:

$$\theta = \cot^{-1}\left(\frac{2ph^2 + hgz_{sd}\sqrt{4z_{sd}^2 + h^2}}{2gz_{sd}^2\sqrt{4z_{sd}^2 + h^2}}\right). \tag{3}$$

With z_{sd} the perpendicular distance between source and detector, and h the detector height, $|DC|$ in Fig. 9. The elaborated derivation of this equation can be found in Supplement 1. The previous equation allows to calculate tilt angle leading to the geometry depicted in Fig. 8(b), based on setup parameters g, h, p, and z_{sd}.

3. Experiments

The performance of the trapezoidal grating was simulated using GATE [37]. GATE is a Monte Carlo software-platform based on Geant4 [38], which is used to simulate radiographs, CT (computed tomography), PET (Positron emission tomography), and SPECT (Single-photon emission computed tomography). In GATE-simulations, a setup is defined, and X-rays are simulated in the form of photon particles. An optics-free X-ray imaging experiment simulation can be configured in GATE by considering an X-ray source, sample, and detector. Recent improvements in GATE allow attenuation, phase, and dark field contrast effects to be modeled, as refraction can now be included in simulations (where the dark field signal is generated by refraction events below the spatial resolution of the imaging setup as long as the micro-structure of the sample is modeled to sufficient detail) [39]. In this study, however, only attenuation and phase contrast was considered, because it was sufficient to demonstrate the concept of multi-resolution EI. For the CT images, the CAD-ASTRA mesh projector was used [40,41], because of its faster execution time. CAD-ASTRA allows simulation of X-ray projections from CAD models through GPU-accelerated ray tracing and supports ray refraction in a geometric optics framework. A GATE macro and a CAD-ASTRA script used for the experiments in this paper, can be found in Supplement 1.

The setup for the EI simulations was adapted to mimic the FleXCT scanner [42,43] at imec Vision Lab, University of Antwerp. The pixel size was 150 µm, and a fixed source-to-detector distance (SDD) of 1800 mm was used in the simulations. The sample grating and sample were translated along the optical axis between 600 mm and 1600 mm from the source, resulting in a magnification between 1.25 and 3.25. The maximal attainable resolution of an EI setup, when

Optics EXPRESS

dithering is applied, corresponds to the aperture width, which varies in this configuration from 10 μm to 25 μm. Each simulation including a sample used 5 dithering steps, with a step size equal to one fifth of the effective period. In the GATE simulations, the source was a polychromatic cone-beam source with a rectangular finite spot-size of 34× 10 μm^2, the spectrum of the source is shown in Fig. 10. To sufficiently block incoming X-rays, gold was chosen as absorbing material for the 225 μm thick grating bars. Each GATE simulation used $2 \cdot 10^8$ photons and the IC was sampled at 5 mask-steps for every flat field and projection. The CAD-ASTRA simulations used a fan-beam source with the same spectrum as the GATE simulations, shown Fig. 10, and a Gaussian spot size with FWHM of 20 μm. The parameters of the trapezoidal grating are shown in Fig. 11. The detector grating was a conventional grating with a period of 149 μm and an aperture of 29.6 μm.

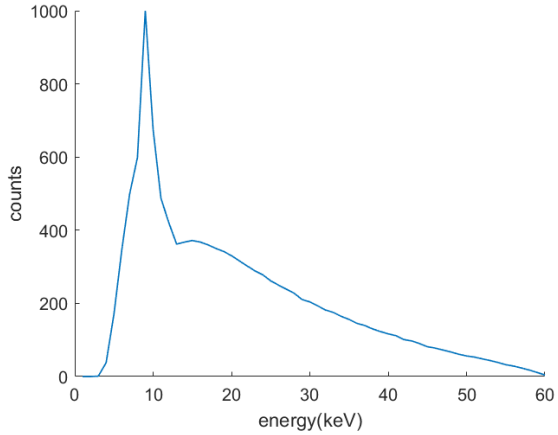

Fig. 10. The spectrum of the polychromatic source that was used in the GATE simulations.

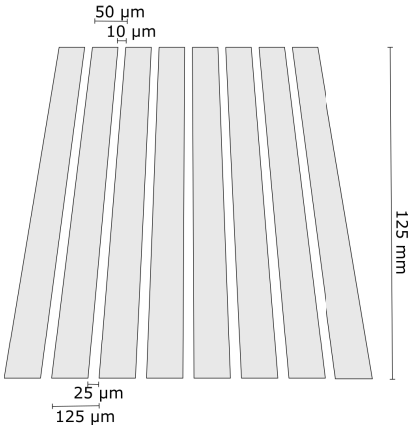

Fig. 11. The geometric parameters of the trapezoidal grating used in the simulations. The number of grating bars is determined by the number of detector pixels.

3.1. Flat field analysis

In the first experiment, the flat field obtained with a tilted trapezoidal grating was studied, as shown in Fig. 12(a). The flat field was projected on a detector grid consisting of 66 × 66 pixels.

Optics EXPRESS

To analyze the expected intensity loss of the tilted trapezoidal grating at different magnifications, GATE-simulation results of a setup with gratings but without a sample were compared between conventional and trapezoidal gratings. The metric that was used to compare the gratings was obtained by dividing the average intensity of a simulation with a trapezoidal grating by the average intensity of a simulation with a conventional grating, for different magnifications and mask-steps.

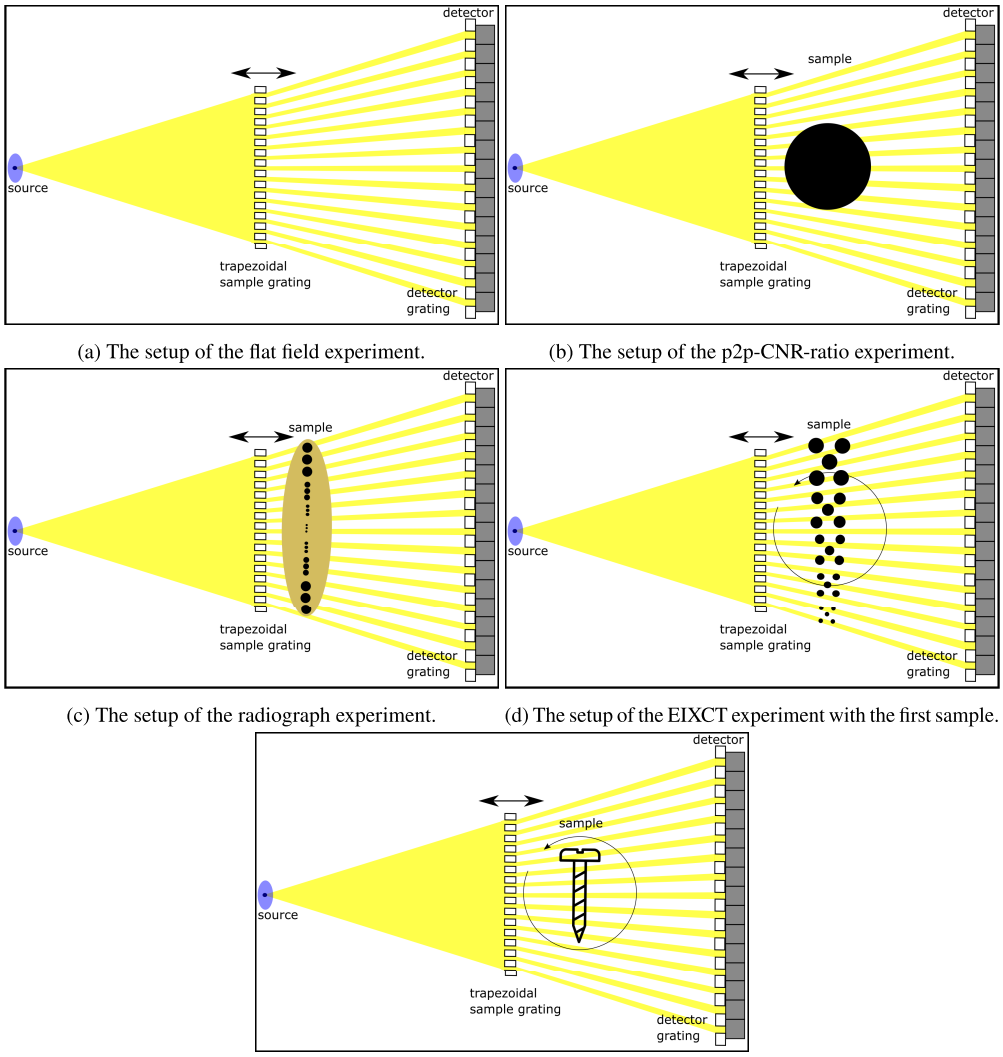

(a) The setup of the flat field experiment.

(b) The setup of the p2p-CNR-ratio experiment.

(c) The setup of the radiograph experiment.

(d) The setup of the EIXCT experiment with the first sample.

(e) The setup of the EIXCT experiment with the second sample.

Fig. 12. The setups of the different simulation experiments.

3.2. Peak-to-peak Contrast-to-noise ratio comparison

In the second experiment, conventional and trapezoidal gratings were compared based on the peak-to-peak contrast-to-noise ratio (p2p-CNR) [22,44] at different magnifications. The p2p-CNR was obtained by performing an EI simulation in GATE of a cylinder, and is calculated by dividing the difference between the two refraction peaks for every row at the edges of the cylinder by the

Optics EXPRESS

variance of the differential phase contrast without sample. The cylinder that was studied in this simulation had a diameter of 4 mm, and was made out of aluminum. The p2p-CNR evaluates the reliability of contrast information in an image, helping to assess whether features can be confidently identified and analyzed despite noise interference. It is an equivalent metric to CNR (contrast-to-noise ratio) for phase contrast imaging. The setup is shown in Fig. 12(b).

3.3. Multi-resolution radiograph of a test phantom

In the third experiment, an EI radiograph of a test phantom was simulated in GATE. The test phantom was a poly-ethylene ellipsoid containing triplets of aluminum cylinders with diameters varying between 10 μm and 50 μm, as shown in Fig. 12(c). To image the sample at multiple magnifications, the grating was positioned on various positions along the optical axis, where it was vertically translated and tilted to match the FOV with a detector grid consisting of 66×66 pixels.

3.4. Computed Tomography of a test phantom

In the fourth experiment, an EIXCT simulation was performed using the trapezoidal grating. Unlike the other experiments, this experiment was simulated using the CAD-ASTRA toolbox. Since only a single axial slice was simulated, the trapezoidal grating was not tilted. Two test phantoms were simulated: a test phantom consisting of groups of 5 aluminum cylinders with varying diameters, as shown in Fig. 12(d), and a steel screw, as shown in Fig. 12(e). The diameters of the cylinders vary between 8 μm and 80 μm. The detector consisted of a single row of 50 pixels, resulting in a FOV varying between 6.7 mm $\times$ 6.7 mm for the lowest magnification to 2.5 mm $\times$ 2.5 mm for the highest magnification. 150 projection angles, equally distributed over a 360° range, were used for every magnification, and the differential phase contrast resulting from the projections was integrated and reconstructed using filtered back-projection, with the iradon function in MATLAB. Due to the limited noise in the CAD-ASTRA simulations, the Ram-lak filter was chosen along with linear interpolation.

4. Results

4.1. Flat field analysis

The results of the flat field experiment are shown in Table 1. Each element in the table is calculated by dividing the average intensity of a simulation with a trapezoidal grating by the average intensity of a simulation with a conventional grating, for the indicated mask-step and magnification. The experiments show that the intensity loss of using a trapezoidal grating compared to using a conventional grating is higher with increased magnification, and that misaligning the grating in mask-stepping further reduces the X-ray flux. While the loss is however never higher than 12%, this reduction can cause a trade-off between resolution range and flux when higher magnifications or misalignments are considered.

Table 1. This table shows the ratio of the average flat field intensity of an EI simulation with conventional gratings and one with a tilted trapezoidal grating. Each row corresponds to a different mask-step.

mask-step	M=1.25	M=1.5	M=2	M=2.4	M=3.25
++	0.97	0.95	0.93	0.92	0.89
+	0.98	0.96	0.94	0.93	0.9
0	0.98	0.97	0.96	0.95	0.92
-	0.98	0.96	0.94	0.93	0.9
- -	0.98	0.95	0.93	0.92	0.88

Optics EXPRESS

4.2. P2p-CNR comparison

The results of the p2p-CNR study are shown in Fig. 13. In Fig. 13(a), the differential phase contrast of the cylinder is shown. Figure 13(b) shows the p2p-CNR values of the imaged cylinder. For each magnification and each grating type, a boxplot is constructed. Each boxplot contains the p2p-CNR values which are calculated for every row. The graph does not show a substantial difference between the conventional and trapezoidal gratings. This experiment shows a strong property of the trapezoidal grating: despite a reduction in flux at higher magnifications, the contrast quality represented by this metric is preserved.

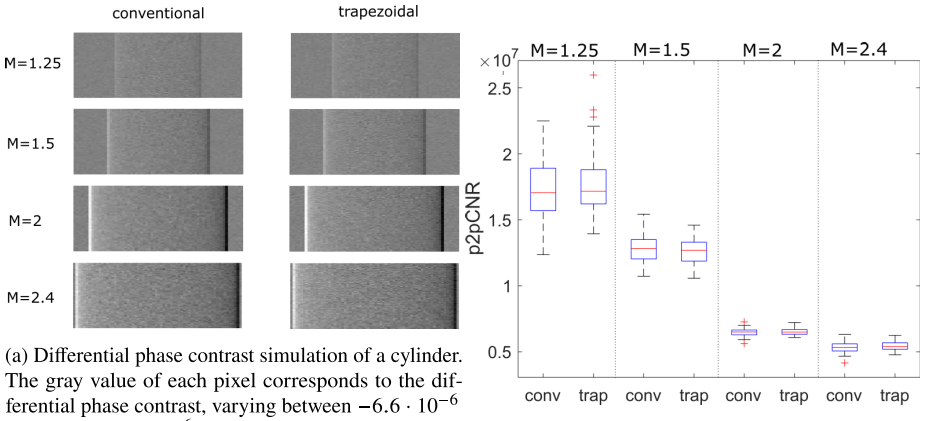

(a) Differential phase contrast simulation of a cylinder. The gray value of each pixel corresponds to the differential phase contrast, varying between $-6.6 \cdot 10^{-6}$ (black) and $2.5 \cdot 10^{-6}$(white).

(b) P2p-CNR ratio.

Fig. 13. The results of the p2p-CNR simulation experiment. Every value in the boxplot of 13(a) corresponds to the p2p-CNR of a row of the corresponding image of 13(b).

4.3. Multi-resolution radiograph of a test phantom

The differential phase contrast radiographs of the test phantom are shown in Fig. 14. At lowest magnification of $M = 1.25$, the whole ellipsoid fits in the FOV, but the nested cylinders cannot be resolved in the differential phase contrast. At magnifications 1.5 and 2, the projected ellipsoid exceeds the FOV, but the largest cylinders at the sides can be resolved. The triplet containing the smallest cylinders in the center, however, can not be resolved. This triplet is slightly visible at a magnification of 2.4, and clearly visible at a magnification of 3.25. This experiment also demonstrates successfully the use of a trapezoidal grating for imaging on a 2D detector grid.

4.4. Computed Tomography of a test phantom

The reconstructed phase contrast slice of the EIXCT simulation experiment is shown in Fig. 15. The red arrows represent equivalent cylinder groups. Once again, the smallest cylinder, imaged on the right in Fig. 15, can only be observed in the simulations with the highest magnifications, while at lower magnifications, a higher FOV is imaged.

Figure 16 shows the phase contrast reconstruction of a screw at different magnifications. The unusual background pattern is caused by the finite amount of sampling rays that CAD-ASTRA uses. At the lowest magnification of $M = 1.28$, as shown in Fig. 16(i), the whole screw is within the FOV. The screw thread is, however, not visible in this image. When the magnification increases, the screw thread becomes increasingly visible and more delineated. These experiments show how our method can be used to image a sample at multiple magnification, selecting the optimal choice between FOV and resolution.

Optics EXPRESS

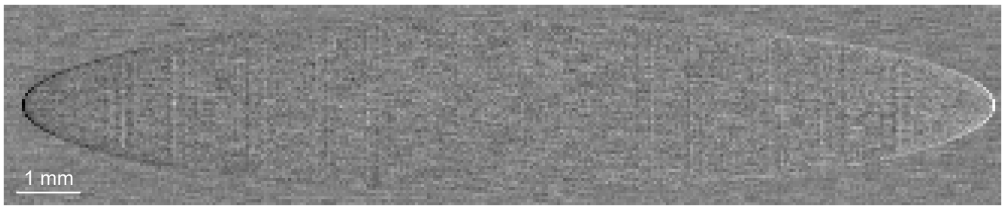

(a) Magnification 1.25

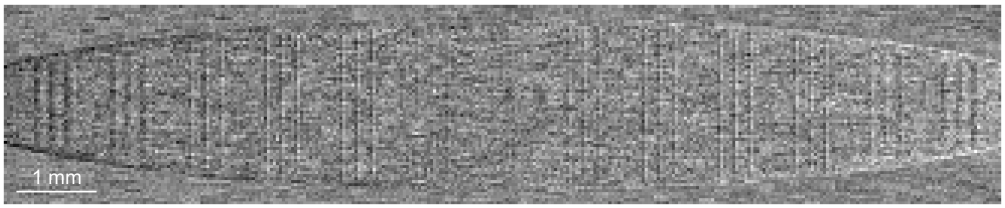

(b) Magnification 1.5

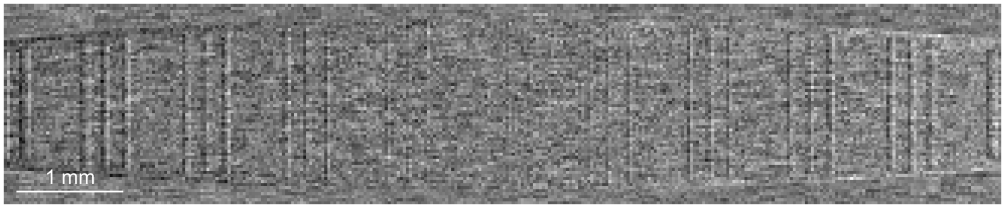

(c) Magnification 2

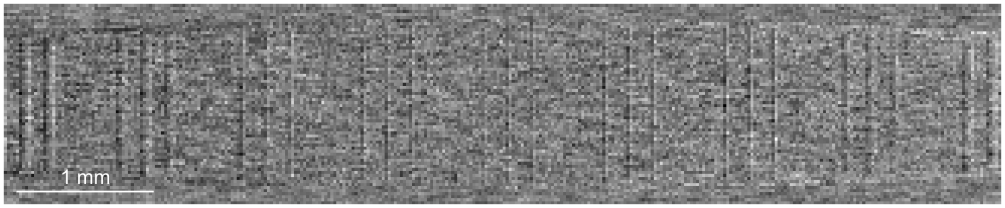

(d) Magnification 2.4

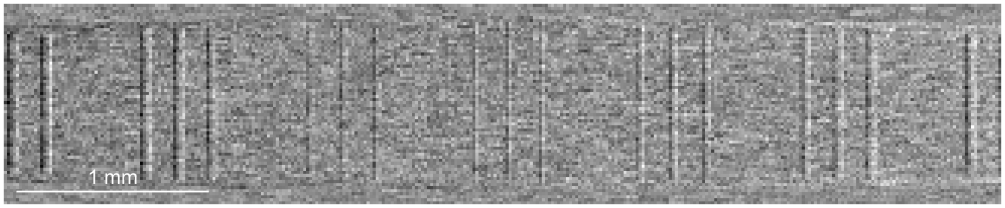

(e) Magnification 3.25

Fig. 14. Differential phase contrast radiograph of the test phantom at different magnifications.The gray value of each pixel corresponds to the differential phase contrast, varying between $-2.4 \cdot 10^{-6}$ (black) and $2.3 \cdot 10^{-6}$(white).

Optics EXPRESS

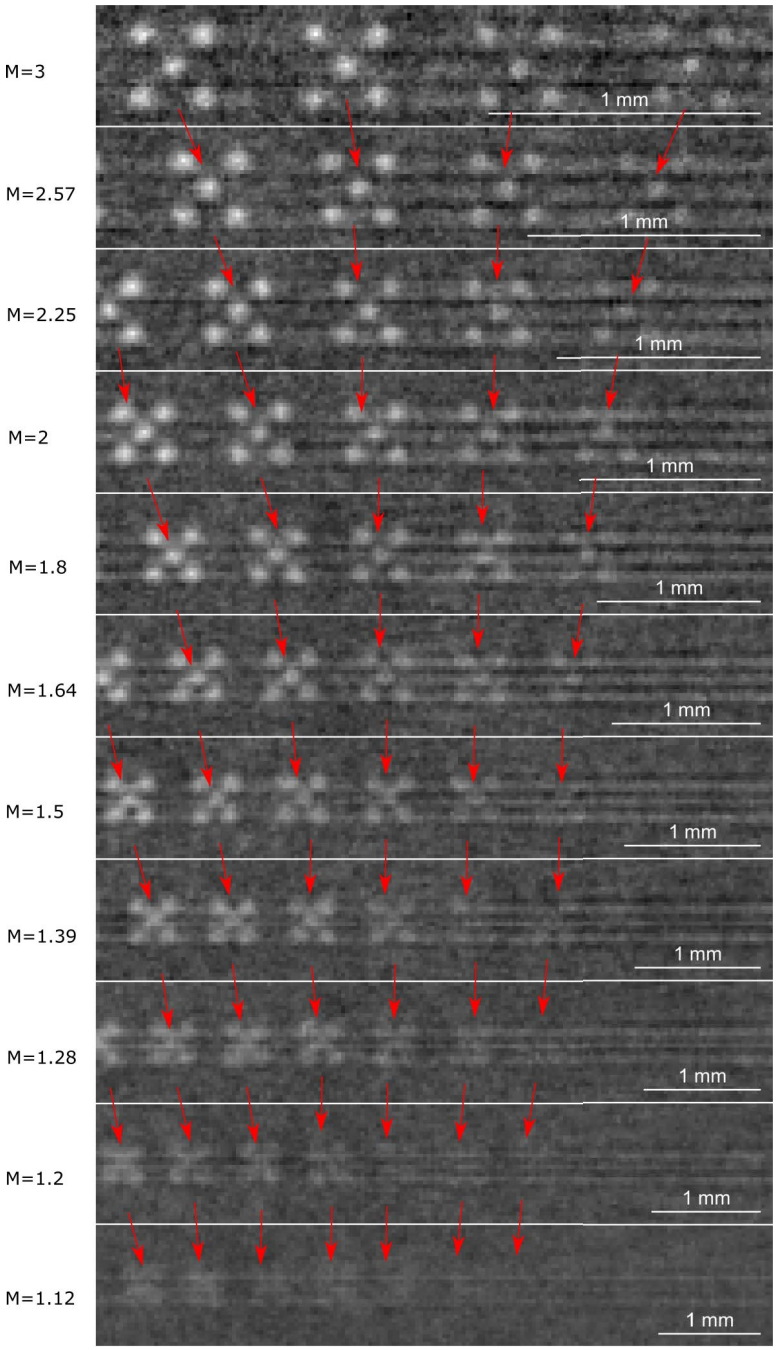

Fig. 15. EIXCT of the test phantom, which consists of groups of five cylinders. The diameter of the cylinder in each group decreases from left to right. Magnification is indicated at each image. The red arrows indicate corresponding groups of cylinders.The gray value of each pixel corresponds to the phase contrast, varying between $-1.0 \cdot 10^{-4}$ (black) and $2.5 \cdot 10^{-4}$(white).

Optics EXPRESS

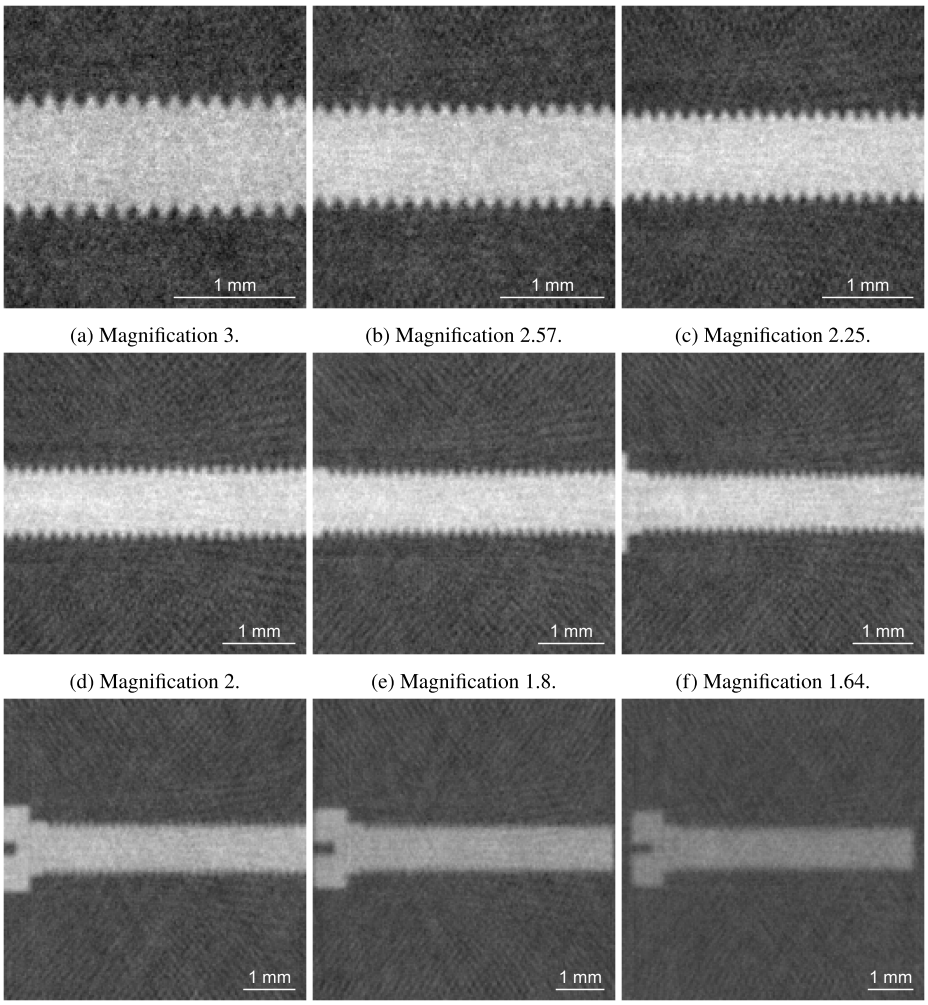

(a) Magnification 3. (b) Magnification 2.57. (c) Magnification 2.25.

(d) Magnification 2. (e) Magnification 1.8. (f) Magnification 1.64.

(g) Magnification 1.5. (h) Magnification 1.39. (i) Magnification 1.28.

Fig. 16. The EI reconstruction of the screw at different magnifications. The FOV varies between 6.7 mm × 6.7 mm for the lowest magnification to 2.5 mm × 2.5 mm for the highest magnification. The gray value of each pixel corresponds to the phase contrast, varying between $-1.3 \cdot 10^{-4}$ (black) and $3.2 \cdot 10^{-4}$(white).

5. Discussion

In this paper a multi-resolution EI approach was studied, which makes use of a trapezoidal grating which can preserve the projected period when the magnification changes over a continuous range of magnifications, and which is tilted to allow imaging on a 2D detector grid. The presented simulation results show that the suggested trapezoidal grating allows for multi-resolution EI from a single experimental configuration, i.e., no optical elements need to be changed. The experiments with the test phantoms illustrate the trade-off between resolution and FOV, and highlight the possibility to perform selective region-of-interest scans. The experiments with the flat field and the 2D radiograph show how tilting the trapezoidal grating results in a 2D FOV. The experiments with the flat field and the p2p-CNR for an aluminum cylinder show that the results obtained with the trapezoidal grating are similar to conventional gratings, and that the flux loss is limited. In

Optics EXPRESS

this study, only attenuation and refraction contrast was considered, because it was sufficient to demonstrate the concept of multi-resolution EI. Samples with sub-resolution micro-structures, resulting in dark field contrast, would make the experiments of this study needlessly complex, but could be considered in future work. While the simulation results are promising, some practical considerations have to be taken in to account. First of all, while the trapezoidal grating allows imaging a sample at different resolutions, the resolution has a lower limit at the pixel size, and an upper limit by the aperture width before diffraction becomes non-negligible. Manufacturing should also be taken into account. Our research group is at this moment investigating how to manufacture a trapezoidal grating at micrometer scale and are discussing the options with specialised companies. Similar to our current conventional grating which consists of sequential gold plating, sequential trapezoids might be necessary for the trapezoidal grating, creating a dotted-line pattern, as shown in Fig. 17. This may cause a certain loss in continuity, which has to be studied further.

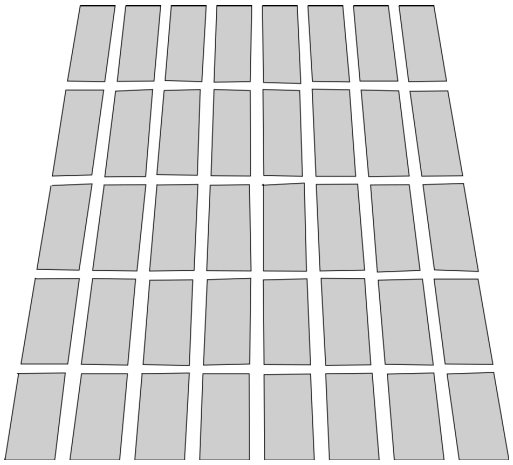

Fig. 17. Dotted line-pattern that may be required when the trapezoidal grating is manufactured.

A trapezoidal grating has to be positioned very carefully into an EI setup, and has to be tilted very precise to achieve optimal alignment. The setup also requires motion of the sample and sample grating along the optical axis to change the magnification, like in conventional CT, as well as vertical motion of the grating to compensate for the difference in magnification. A careful selection of movement stages with the required range and precision is required, along with a specific alignment strategy. From aligning the trapezoidal grating in this simulation study, we noticed that a rotational misalignment around the 'tilting' axis of around 20 arc seconds can severely reduce the image quality, and rotational misalignment of around 1 arc minute results in unusable images for the selected FOV. Another element to take into account is the influence of translating along the optical axis on the illumination curve. While studying the trapezoidal grating, it was observed that moving the grating closer towards the source changes the width of the ICs, changing the sensitivity for the different contrasts. For setup stability, mask-stepping with the detector grating is advised, and the range of the grating displacement should be adapted to the magnification. This study can be further elaborated by validating the grating with real data in the FleXCT setup [42,43], optimizing the grating parameters, and working out an alignment strategy.

Optics EXPRESS

6. Conclusion

Current EI setups, with conventional one-dimensional line aperture gratings, have a fixed resolution, which is determined by the period and aperture of the grating positioned upstream of the sample. In this paper, a novel trapezoidal grating geometry was introduced that allows EI at a continuous range of resolutions, and is tilted to allow imaging on a 2D detector grid. The grating was evaluated using GATE and CAD-ASTRA simulations. The trapezoidal gratings shows similar performance compared to a conventional grating in the experiments based on flat field intensity and p2p-CNR. The experiments with test phantoms show that this trapezoidal grating allows to perform multi-resolution EI from a single experimental configuration for a continuous range of magnifications, and demonstrates the tilting concept. Introduction of trapezoidal gratings can greatly improve the flexibility of EI, which is an important step towards a generic and flexible EI setup in the future.

Funding. Agentschap Innoveren en Ondernemen (HBC.2020.2159); Fonds Wetenschappelijk Onderzoek (G094320N, G090020N, S003421N).

Acknowledgments. This research was supported by Research Foundation - Flanders (FWO) and Agentschap Innoveren & Ondernemen (Vlaio).

Disclosures. The authors declare no conflicts of interest.

Data availability. Data underlying the results presented in this paper are not publicly available at this time but may be obtained from the authors upon reasonable request.

Supplemental document. See Supplement 1 for supporting content.

References

1. A. Olivo, "Edge-illumination x-ray phase-contrast imaging," J. Phys.: Condens. Matter **33**, 363002 (2021).
2. U. Bonse and M. Hart, "An X-ray interferometer," Appl. Phys. Lett. **6**(8), 155–156 (1965).
3. A. Bravin, "Exploiting the x-ray refraction contrast with an analyser: the state of the art," J. Phys. D: Appl. Phys. **36**(10A), A24–A29 (2003).
4. T. E. Gureyev, S. C. Mayo, D. E. Myers, *et al.*, "Refracting Rontgen's rays: Propagation-based x-ray phase contrast for biomedical imaging," J. Appl. Phys. **105**(10), 102005 (2009).
5. A. Olivo and E. Castelli, "X-ray phase contrast imaging: From synchrotrons to conventional sources," Rivista del Nuovo Cimento **37**, 467–508 (2014).
6. A. Momose, S. Kawamoto, I. Koyama, *et al.*, "Demonstration of X-Ray Talbot interferometry," Jpn. J. Appl. Phys. **42**(Part 2, No. 7B), L866–L868 (2003).
7. C. David, B. Nöhammer, H. Solak, *et al.*, "Differential x-ray phase contrast imaging using a shearing interferometer," Appl. Phys. Lett. **81**(17), 3287–3289 (2002).
8. T. P. Millard, M. Endrizzi, K. Ignatyev, *et al.*, "Method for automatization of the alignment of a laboratory based x-ray phase contrast edge illumination system," Rev. Sci. Instrum. **84**(8), 083702 (2013).
9. M. Longo, L. Rigon, F. C. M. Lopez, *et al.*, "A simplified edge illumination set-up for quantitative phase contrast mammography with synchrotron radiation at clinical doses," Phys. Med. Biol. **60**(3), N21–N34 (2015).
10. F. Schaff, C. Jud, M. Dierolf, *et al.*, "Feasibility of dark-field radiography to enhance detection of nondisplaced fractures," Radiology **311**(2), e231921 (2024).
11. K. Ignatyev, P. R. Munro, D. Chana, *et al.*, "A new generation of x-ray baggage scanners based on a different physical principle," Materials **4**(10), 1846–1860 (2011).
12. A. Gibson, K. E. Piquette, U. Bergmann, *et al.*, "An assessment of multimodal imaging of subsurface text in mummy cartonnage using surrogate papyrus phantoms," Heritage Sci. **6**(1), 7 (2018).
13. M. Endrizzi, B. Murat, P. Fromme, *et al.*, "Edge-illumination x-ray dark-field imaging for visualising defects in composite structures," Composite Structures **134**, 895–899 (2015).
14. B. K. Blykers, C. Organista, M. Kagias, *et al.*, "Exploration of the x-ray dark-field signal in mineral building materials," J. Imaging **8**(10), 282 (2022).
15. H. Lim, J. Lee, S. Lee, *et al.*, "Low-density foreign body detection in food products using single-shot grid-based dark-field x-ray imaging," J. Food Eng. **335**, 111189 (2022).
16. A. Olivo and R. Speller, "A coded-aperture technique allowing x-ray phase contrast imaging with conventional sources," Appl. Phys. Lett. **91**, 074106 (2007).
17. C. K. Hagen, P. C. Diemoz, M. Endrizzi, *et al.*, "Quantitative edge illumination x-ray phase contrast tomography," Proc. SPIE **9212**, 921205 (2014).
18. K. Ignatyev, P. R. T. Munro, R. D. Speller, *et al.*, "Phase contrast imaging with coded apertures using laboratory-based x-ray sources," in *10TH international conference on X-ray microscopy, vol. 1365 of AIP Conference Proceedings* I. McNulty, C. Eyberger, and B. Lai, eds. (2011), pp. 254–257.

Optics EXPRESS

19. G. K. Kallon, M. Wesolowski, F. A. Vittoria, *et al.*, "A laboratory based edge-illumination x-ray phase-contrast imaging setup with two-directional sensitivity," Appl. Phys. Lett. **107**(20), 204105 (2015).
20. L. Massimi, J. A. Meganck, R. Towns, *et al.*, "Evaluation of a compact multicontrast and multiresolution x-ray phase contrast edge illumination system for small animal imaging," Med. Phys. **48**(1), 376–386 (2021).
21. M. Endrizzi, A. Astolfo, F. A. Vittoria, *et al.*, "Asymmetric masks for laboratory-based x-ray phase-contrast imaging with edge illumination," Sci. Rep. **6**(1), 25466 (2016).
22. P.-J. Vanthienen, J. Sanctorum, B. Huyge, *et al.*, "Grating designs for cone beam edge illumination x-ray phase contrast imaging: a simulation study," Opt. Express **31**(17), 28051–28064 (2023).
23. P. Diemoz, M. Endrizzi, C. Hagen, *et al.*, "Angular sensitivity and spatial resolution in edge illumination x-ray phase-contrast imaging," Nucl. Instrum. Methods Phys. Res., Sect. A **784**, 538–541 (2015).
24. P. R. T. Munro, K. Ignatyev, R. D. Speller, *et al.*, "Phase and absorption retrieval using incoherent x-ray sources," Proc. Natl. Acad. Sci. U. S. A. **109**(35), 13922–13927 (2012).
25. A. R. Zekavat, G. Lioliou, O. R. i Morgó, *et al.*, "Phase contrast micro-ct with adjustable in-slice spatial resolution at constant magnification," Phys. Med. Biol. **69**(10), 105017 (2024).
26. J. Vijayakumar, H. Dejea, A. Mirone, *et al.*, "Multiresolution phase-contrast tomography on bm18, a new beamline at the european synchrotron radiation facility," Synchrotron Radiation News 1–10 (2024).
27. R. P. Xian, C. L. Walsh, S. E. Verleden, *et al.*, "A multiscale x-ray phase-contrast tomography dataset of a whole human left lung," Sci. Data **9**(1), 264 (2022).
28. L. Arana Peña, S. Donato, D. Bonazza, *et al.*, "Multiscale x-ray phase-contrast tomography: From breast ct to micro-ct for virtual histology," Physica Medica **112**, 102640 (2023).
29. S. Savatović, M.-C. Zdora, F. D. Marco, *et al.*, "Multi-resolution x-ray phase-contrast and dark-field tomography of human cerebellum with near-field speckles," Biomed. Opt. Express **15**(1), 142–161 (2024).
30. P.-J. Vanthienen, N. Francken, J. Sijbers, *et al.*, "Multi-resolution gratings for edge illumination x-ray phase contrast imaging: a simulation study," *Developments in X-Ray Tomography XV*, vol. 13152 B. Müller and G. Wang, eds., International Society for Optics and Photonics (SPIE, 2024), p. 1315208.
31. T. P. Millard, M. Endrizzi, P. C. Diemoz, *et al.*, "Monte carlo model of a polychromatic laboratory based edge illumination x-ray phase contrast system," Rev. Sci. Instrum. **85**(5), 053702 (2014).
32. S. Wilkins, T. Gureyev, D. Gao, *et al.*, "Phase-contrast imaging using polychromatic hard x-rays," Nature **384**(6607), 335–338 (1996).
33. P. R. T. Munro, K. Ignatyev, R. D. Speller, *et al.*, "The relationship between wave and geometrical optics models of coded aperture type x-ray phase contrast imaging systems," Opt. Express **18**(5), 4103–4117 (2010).
34. A. Peterzol, A. Olivo, L. Rigon, *et al.*, "The effects of the imaging system on the validity limits of the ray-optical approach to phase contrast imaging," Med. Phys. **32**(12), 3617–3627 (2005).
35. L. Massimi, T. Partridge, A. Astolfo, *et al.*, "Optimization of multipoint phase retrieval in edge illumination X-ray imaging A theoretical and experimental analysis," Med. Phys. **48**(10), 5884–5896 (2021).
36. A. Olivo and R. Speller, "Modelling of a novel x-ray phase contrast imaging technique based on coded apertures," Phys. Med. Biol. **52**(22), 6555–6573 (2007).
37. S. Jan, G. Santin, D. Strul, *et al.*, "GATE: a simulation toolkit for PET and SPECT," Phys. Med. Biol. **49**(19), 4543–4561 (2004).
38. S. Agostinelli, J. Allison, K. Amako, *et al.*, "Geant4-a simulation toolkit," Nucl. Instrum. Methods Phys. Res., Sect. A **506**(3), 250–303 (2003).
39. J. Sanctorum, J. De Beenhouwer, and J. Sijbers, "X-ray phase contrast simulation for grating-based interferometry using GATE," Opt. Express **28**(22), 33390–33412 (2020).
40. P. Paramonov, N. Francken, J. Renders, *et al.*, "CAD-ASTRA: a versatile and efficient mesh projector for x-ray tomography with the astra-toolbox," Opt. Express **32**(3), 3425–3439 (2024).
41. N. Francken, J. Sanctorum, P. Paramonov, *et al.*, "Edge illumination x-ray phase contrast simulations using the CAD-ASTRA toolbox," Opt. Express **32**(6), 10005–10021 (2024).
42. B. De Samber, J. Renders, T. Elberfeld, *et al.*, "FleXCT: a flexible X-ray CT scanner with 10 degrees of freedom," Opt. Express **29**(3), 3438–3457 (2021).
43. B. Huyge, P. Vanthienen, N. Six, *et al.*, "Adapting an XCT-scanner to enable edge illumination x-ray phase contrast imaging," in *Proceedings of the 12th Conference on Industrial Computed Tomography (iCT) 2023*, E-Journal of Nondestructive Testing Vol. 28(3), 1–7 (2023).
44. J. Sanctorum, N. Six, J. Sijbers, *et al.*, "Augmenting a conventional x-ray scanner with edge illumination-based phase contrast imaging: how to design the gratings," Proc. SPIE **12242**, 1224218 (2022).